ADVANCED FUNCTIONAL MATERIALS
www.afm-journal.de

Chimie Douce Derived Novel P2-Type Layered Oxide for Potassium-Ion Batteries

*Pawan Kumar Jha, Alexander Golubnichiy, Dorothy Sachdeva, Abhik Banerjee, Gopalakrishnan Sai Gautam, Maximilian Fichtner, Artem M. Abakumov, and Prabeer Barpanda**

The emergence of K-ion batteries (KIBs) heralds a promising frontier in energy storage technology, offering the potential for high specific energy density, long cycle life, and robust power capabilities, all while utilizing the abundant resources of potassium. In response to the challenges posed by synthetic intricacies related to K-based cathodes, the effort is directed toward employing soft chemistry (*chimie douce*) method to unveil a *hitherto-unknown* P2-type $K_{1/3}Co_{1/3}Mn_{2/3}O_2$ (KCM) layered oxide cathode for KIBs. Comprehensive analysis using diffraction, microscopy, and spectroscopy tools reveals the ion exchange reaction proceeds through overlay ordered structure formation mechanism. The as-prepared KCM material serves as a ≈2.9 V positive K^+ insertion host. Further, it showcases an exceptional structural reversibility, robust cycling performance with ≈100% coulombic efficiency even after 100 cycles, and maintaining electrochemical stability even at elevated temperature (c.a. 40° and 50 °C). The KCM cathode exhibits in-plane Co–Mn ordering and solid-solution redox mechanism during (de)potassiation. Combining first-principles calculations with experimental tools, this research demonstrates the efficacy of ambient ion-exchange route in stabilizing promising cathode materials for KIBs. This innovative synthetic approach not only streamlines synthetic complexities, but also holds significant implications for the advancement of KIB technology for stationary energy storage.

1. Introduction

Lithium-ion batteries (LIBs) are widely used in the energy storage landscape, encompassing applications ranging from stationary grid storage to electric vehicles as they offer efficient cycle life, high energy/power density, and reliable operation.[1] Nevertheless, the widespread adoption of LIBs faces several constraints, including increasing global energy demands, safety concerns, and the limited availability and non-uniform geographical distribution of lithium-based resources.[2] Consequently, it becomes imperative to design and develop alternative battery technologies offering comparable energy densities, similar chemistry, cost-effectiveness, and enhanced safety.[3] In contrast to sodium and other multivalent alternative systems, potassium-ion batteries (KIBs) can cater to cost-effective, large-scale stationary grid storage applications. The relatively small Stokes radius of K^+ ions results in weaker interactions with solvents and anions, thereby facilitating faster ionic mobility within the electrolyte and charge transfer at

P. K. Jha, P. Barpanda
Faraday Materials Laboratory (FaMaL)
Materials Research Center
Indian Institute of Science
Bangalore 560012, India
E-mail: prabeer@iisc.ac.in

A. Golubnichiy, A. M. Abakumov
Center for Energy Science and Technology
Skolkovo Institute of Science and Technology
Bolshoi blv. 30–1, Moscow 121205, Russia

D. Sachdeva
Materials Research Centre
Indian Institute of Science
Bangalore 560012, India

A. Banerjee
Research Institute for Sustainable Energy (RISE)
TCG Centres for Research and Education in Science and Technology
Sector V, Salt Lake, Kolkata 700091, India

G. Sai Gautam
Department of Materials Engineering
Indian Institute of Science
Bangalore 560012, India

M. Fichtner, P. Barpanda
Helmholtz Institute Ulm (HIU)
Electrochemical Energy Storage
89081 Ulm, Germany

M. Fichtner, P. Barpanda
Institute of Nanotechnology
Karlsruhe Institute of Technology (KIT)
76021 Karlsruhe, Germany

The ORCID identification number(s) for the author(s) of this article can be found under https://doi.org/10.1002/adfm.202410665

DOI: 10.1002/adfm.202410665

electrode/electrolyte interface.[3a,4] Further, reversible intercalation of K^+ into graphite anodes renders it a favorable choice for energy storage systems.[5] Finally, K/K^+ exhibits a lower standard electrode potential compared to Li/Li^+ (−0.1 V *vs.* Li) in carbonate ester solvents such as propylene carbonate (PC; KPF_6) and ethylene/diethyl carbonate (EC: DEC; KPF_6).[5] This imparts KIBs with the broadest potential window of ≈4.6 V, compared to the 4.5 and 4.2 V potentials for Li and Na, respectively, without necessitating the inimical K metal plating on the anode side.[6] For practical realization of KIBs, it is crucial to develop robust framework host materials that can effectively serve as the positive electrodes (cathodes).

The bigger ionic size of K^+ (1.38 Å), compared to Na^+ (1.02 Å) and Li^+ (0.76 Å), poses a formidable challenge in the quest to identify suitable cathode materials for KIBs.[3a,7] Indeed, strong intralayer electrostatic repulsion between the K^+ ions imparts different stabilizing chemistry on diverse structural configurations that deviate significantly from their Li and Na analogs. Exploration of potential cathodes for KIBs has revolved around four specific material types: classical layered transition metal(s) oxides, polyanionic frameworks, Prussian blue analogs, and organic polycyclic compounds.[3a,4a,8] Among them, layered oxide materials have emerged as viable cathode candidates in KIBs because of their relatively larger interlayer distance, swift K^+ migration within a 2D open framework, and ability to accommodate considerable number of K^+ ions.[8,9] However, strong intralayer electrostatic $K^+ - K^+$ repulsion leads to low K concentrations in the crystal framework. As a result, direct synthesis methods often yield phases with a low potassium content (leading to low capacity), and their tendency to transform into other thermodynamically stable phases when treated at high temperatures.[7,10] Thus, the preparation of stable layered 3*d* transition metal-based P2-type phases with a high K-content remains a formidable task when utilizing direct synthesis routes that inevitably lead to the formation of K deficient P3-type structures.

In this pursuit, an intriguing approach involves the cation exchange reaction, in which K^+ substitute Na^+ within sodium-based compounds. For instance, electrochemical ion exchange technique can form P2-type K_xCoO_2 and $K_xNi_{1/3}Mn_{2/3}O_2$ compounds in potassium half-cell (*vs.* K/K^+) by first charging the corresponding Na-based transition metal oxides using K-based electrolyte.[11] Further, Hwang et al.[12] adopted a similar approach to yield P3-type K_xCrO_2 from O3-$NaCrO_2$. These previous studies enable the exploration of new compounds as cathode materials in KIBs. Nonetheless, electrochemical synthesis is a complicated process for producing bulk materials, rendering it practically unfeasible. These issues inspired our efforts to address the synthetic complexities by adopting soft chemistry (*chimie douce*) ion exchange approach to developed P2-type oxide compounds for K-ion batteries.

Herein, we introduce a novel P2-type $K_{1/3}Co_{1/3}Mn_{2/3}O_2$ (KCM) layered compound using ambient *chimie douce* cation exchange as a stable cathode for KIBs operating at ambient and high temperatures. We have comprehensively explored the cation exchange progress using suites of analytical tools. Further, we have investigated the KCM product focusing on its structural, morphological, electronic, and electrochemical properties. Electrochemical tests versus K/K^+ revealed that KCM can be harnessed as a positive K^+ insertion host operating at ≈2.9 V comprising Co and Mn redox-active centers. Ex situ and electrochemical characterization elucidate the pure solid solution (single-phase) behavior during (de)potassiation. In addition, it exhibits exceptional structural reversibility, robust cycling performance, and ≈100% coulombic efficiency, even after 100 cycles. The electrochemical performance is notably stable and efficient even at elevated temperatures (c.a. 40° and 50° C). By synergizing first-principles calculations with a comprehensive array of experimental characterizations, the current work attests the efficacy of ambient soft chemistry ion-exchange reactions in synthesizing metastable phases derived from their sodium analogs. This has led to the identification of P2-type $K_{1/3}Co_{1/3}Mn_{2/3}O_2$ as a robust cathode insertion material for KIBs apt for stationary storage. Finally, this material discovery opens a new dimension in the context of cathode material design for KIBs.

2. Results and Discussion

2.1. Ion Exchange Mechanism and Physical Characterization

The synthesis of the KCM compound from the parent NCM phase was accomplished via the ambient ion exchange route,[13] as illustrated in Figure S1 (Supporting Information) (refer to the Experimental Section for detailed procedures). A series of XRD patterns spanning from t = 0 to t = 12 h is presented in **Figure 1a** and Figure S2 (Supporting Information), elucidating the structural evolution of the sample over the course of the reaction and the progress of Na^+ with K^+ substitution within the crystal framework. The distinctive alterations in the structure are discernible, particularly in the vicinity of the initial 002 peak. Notably, immediately upon the initiation of the reaction process (at 15 s), the appearance of small peaks at 14.1° and 39.5° 2θ signifies the commencement of structural changes, with the intensity of these newly formed peaks increasing over time. After 15 min of the reaction, additional peaks at 12.8°, 21.2°, and 25.6° 2θ emerge, indicating further structural rearrangement with progressive K^+ insertion and Na^+ removal. After 2 h, the complete disappearance of the peaks corresponding to the parent NCM phase is observed, and the intensity of the peak at 12.8° 2θ further increases. Through continued reaction and increased K-intercalation, peaks associated with the intermediate phase gradually vanish, and by the end of 12 h, phase pure KCM product becomes evident. Consequently, the entire ion-exchange process can be delineated into three stages. The initial stage involves the rapid formation of the intermediate phase, followed by the second stage characterized by the emergence of the final KCM phase and the disappearance of the parent NCM phase. In the final stage, there is a gradual increase in the intensity of the final KCM phase and a reduction in the intensity of the intermediate phase. The appearance of new peaks in proximity to the 002 peaks at lower angles indicates an increase in the interlayer slab spacing during a structural rearrangement process, indicative of K^+ insertion into the layered framework.

The crystal structures of parent NCM and target KCM phases were analyzed by Rietveld refinement from lab and synchrotron X-ray powder diffraction (SXRD: at SLRI, Thailand) of $\lambda = 1.54$ Å (source: Cu Kα1) and $\lambda = 1.033$ Å respectively (Figure 1b,c) using the FullProf suite. Reliable refinement was achieved assuming a hexagonal structure with space group $P6_3/mmc$, as presented

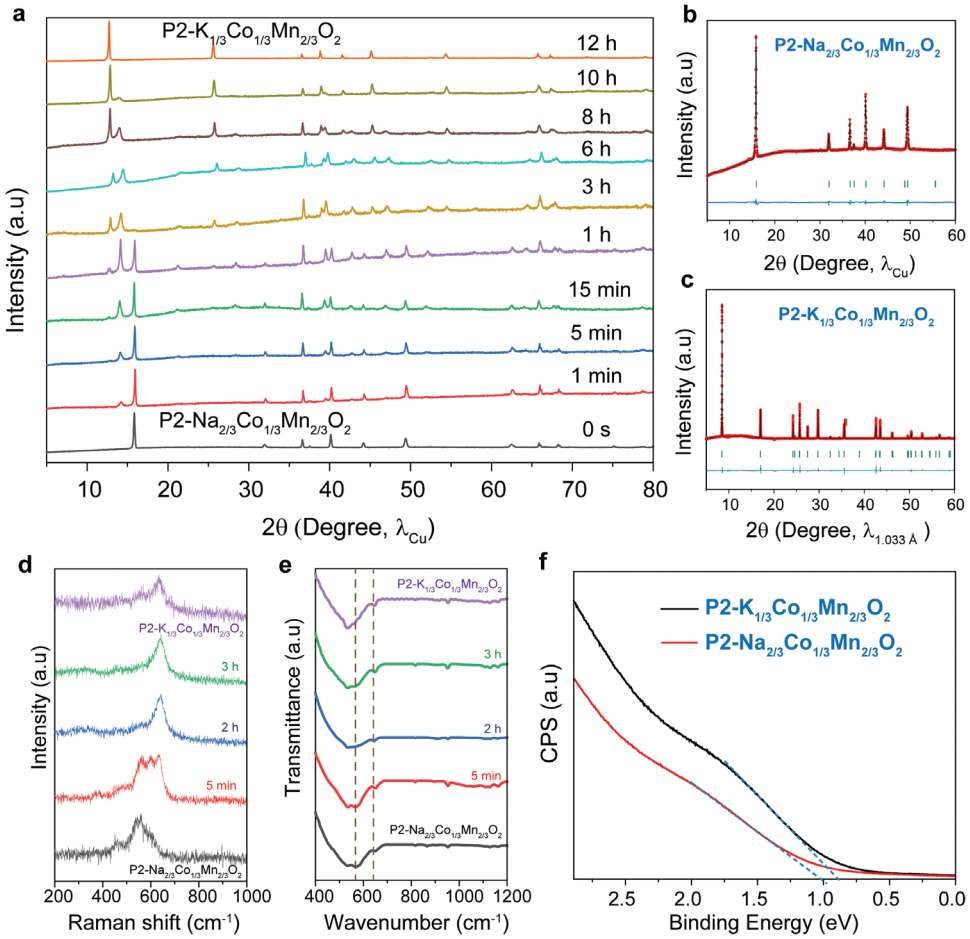

Figure 1. a) XRD patterns illustrating the dynamic structural evolution during ion-exchange (from Na to K) reaction at ambient condition. Rietveld refined b) powder XRD pattern (λ = 1.5405 Å) of parent P2-type $Na_{2/3}Co_{1/3}Mn_{2/3}O_2$ and c) synchrotron X-ray powder diffraction pattern (λ = 1.033 Å) of target P2-type $K_{1/3}Co_{1/3}Mn_{2/3}O_2$ product assuming hexagonal crystal structure (s.g. $P6_3/mmc$). The experimental data (red dots), calculated pattern (black line), their difference curve (blue line), and Bragg diffraction positions (green ticks) are shown. Comparative d) Raman and e) FT-IR spectra at different stages of ion exchange reaction. f) UPS photoelectron signals (plotted with respect to the Fermi level) showing the expanded region near the Fermi level.

in Tables S1 and S2 (Supporting Information). The diffraction peaks in both phases can be indexed to a hexagonal unit cell corresponding to P2 nomenclature as proposed by Delmas et al.[14] The crystal structure comprises of alternating layers of $(MO_2)_n$ slabs built from MO_6 edge-sharing octahedra. In between these layers, K^+/Na^+ ions occupy triangular prismatic oxygen coordination environments. This structure follows the ABBA type of oxygen layer stacking sequence with the periodicity of four oxygen layers. In this type of oxygen framework, two distinct types of KO_6 prisms are possible: one that only shares faces (K_f) and the other that only shares edges (K_e) with the MO_6 octahedra above and below. The occupancy of K^+ at the K_e and K_f sites is intricately influenced by the optimization of site energy, electrostatic interactions, as well as charge and magnetic orderings within the crystal lattice. Notably, the K_f site shares faces with transition metal octahedra, resulting in heightened electrostatic repulsion from transition metal ions.[15] However, this repulsion is counteracted by the minimization of electrostatic repulsion between K^+ ions. Further, a pronounced increase in the lattice parameter c is observed, transitioning from 11.21 Å for NCM to 13.96 Å after K^+ ion exchange, signifying the expansion of the K-metal layer and the enlargement of $d_{(O\text{-}K\text{-}O)}$ distances capable of accommodating the larger-sized K^+ ions.[15b,16] Additionally, we observed a net ≈25% volume change during the topotactic ion-exchange reaction from the parent NCM to the final KCM phase. This expansion aligns with the characteristics observed in other typical P2-type layered K-based compounds.[10c,17] While a subtle increment in the lattice parameters a and b is discernible, the overarching trend emphasizes the structural adjustments facilitating the accommodation of K^+ within the crystal lattice. Importantly, once formed through exchange process, the target phase remains stable up to 900 °C (Figure S3a, Supporting Information). However, attempts to directly synthesize this compound using the solid-state route at various temperatures resulted in the formation of thermodynamically stable P3-type phases at both 800 and 900 °C (Figure S3b, Supporting Information).

Vibrational spectroscopic techniques, namely Raman scattering (RS) spectroscopy and Fourier transform infrared (FT-IR) spectroscopy, were employed to probe the local environment within the crystal framework. The corresponding spectra

are presented in Figure 1d,e, respectively. The Raman spectra (Figure 1d) of the parent NCM exhibit characteristic active bands, namely E_g and A_{1g}, at ≈460 and 548 cm^{-1}, respectively.[18] Upon a 5 min-long ion exchange reaction, the Raman bands shift toward higher frequencies accompanied by the emergence of new bands at 635, 601, and 504 cm^{-1}, respectively. The appearance of these new bands during K^+ insertion suggests potential Na–K cation ordering during the ion-exchange process, as well as an increased interlayer spacing in the layer where K substitutes Na. Subsequent stages of the ion exchange reaction led to further shifts in the Raman bands to higher frequencies, resulting in the complete disappearance of the initial bands corresponding to the parent NCM. Upon eventual completion of reaction, distinct A_{1g} and E_g bands characteristic of the layered KCM phase are observed. Importantly, the observed shift of Raman bands upon K^+ insertion is attributed to the larger interlayer distances associated with the expanded K^+ layer. This structural modification serves to alleviate the repulsion between adjacent KO_2 slabs, facilitating a more localized electron distribution within the MO_2 slabs and, consequently, a heightened repulsion between adjacent MO_2 slabs.[15b,19] Parallel behavior is discerned in the FT-IR spectra, as depicted in Figure 1e, where the ion exchange of Na with K induces small shifts in the Co–O/ Mn–O bands. The X-ray photoelectron spectra (XPS) (Figure S4 and Table S3, Supporting Information) of the parent NCM and the final product KCM phase revealed the electronic configuration of Co remained unchanged, maintaining its 3+ oxidation state during the ion-exchange process. Conversely, Mn exhibited a shift in oxidation state from the initial mixed state of 3+/4+ in the NCM compound to a 4+ state in the final KCM compound. Importantly, the observed oxidation of Mn during the ion-exchange process suggests a lower concentration of K^+ ions and more vacancies present at the alkali-ion site in comparison to the parent compound. In addition, Figure 1f and Figure S5 (Supporting Information) present the UPS photoelectron spectra with respect to Fermi level and expanded region near the Fermi level, respectively. The heightened intensity of the peaks observed in the NCM case signifies a higher density of *d* band states, suggesting the existence of Mn^{3+} or more filled *d* band, consistent with our XPS results. The measured lower valence band edge (VBE) of 0.91 eV for the KCM phase as compared to 1.05 eV for the parent NCM phase hints at a little lower voltage for the final phase.

Both the parent NCM and the final KCM display similar flake-like microstructure with particle size ranging from 2 to 4 µm, as depicted in Figure S6a,b (Supporting Information). Elemental mapping using SEM-EDS confirms the uniform distribution of constituent elements, including K(Na), Co, Mn, and O, within the KCM (NCM) structure (Figure S6c,d, Supporting Information).

Following, the local structure of the parent NCM, target KCM and the intermediate phase formed at 3 h of the cation exchange were characterized with transmission electron microscopy. Selected area electron diffraction (SAED) patterns of the NCM phase were consistently indexed with a hexagonal unit cell with $a \approx 2.8$ Å, $c \approx 11.2$ Å, in agreement with the results of the Rietveld refinement (Figure S3a,b, Supporting Information). The *hhl*, $l = 2n$ reflection condition is obvious from the [1$\bar{1}$0] SAED pattern (Figure S3b, Supporting Information) corroborating the $P6_3/mmc$ space group. [010] and [1$\bar{1}$0] HAADF-STEM images of the parent NCM phase confirm the P2 structure (Figure S4, Supporting Information) as the layers of the (Co, Mn) atomic columns in the [010] HAADF-STEM image demonstrates no lateral displacements specific to the P2 stacking sequence. The images show no visible sign of the Na and (Co, Mn) antisite disorder. STEM-EDX analysis demonstrates the cation ratio of Na:Co:Mn = 0.66(3):0.35(1):0.66(1), in good agreement with the nominal composition and ratio obtained through ICP-OES (Inductively Coupled Plasma – Optical Emission Spectrometry) for Na:Co:Mn = 0.66:0.34:0.66.

The cation exchange for 3 h results in leaching of nearly 0.4 Na, but insertion of only ≈0.2 K yielding the cation ratio of Na:K:Co:Mn = 0.25(2):0.19(1):0.346(3):0.654(3) that corresponds to the more cation-deficient $(Na,K)_{0.45}Co_{1/3}Mn_{2/3}O_2$ (NKCM) formula compared to that of the parent NCM compound. Two remarkable features appear in the SAED patterns of this intermediate NKCM phase. The symmetry-forbidden 00*l*, $l \neq 2n$ reflections, barely visible in the [010] SAED pattern of NCM due to multiple diffraction, appear much brighter and significantly elongated along c* in the same pattern of NKCM (marked with black arrowheads in Figure S7, Supporting Information). At the same time, all reflection rows in both the [010] and [1$\bar{1}$0] SAED patterns of NKCM become streaked with diffuse intensity lines (Figure S7c,d, Supporting Information). It indicates the layers which were symmetry-related in NCM because of the 6_3 screw axes become different in NKCM, but alternation of these layers along the *c*-axis is not perfect and contains numerous faults causing the diffuse intensity lines (Figure S8, Supporting Information). Additionally, extra weak diffuse intensity lines at the ±n/3[11*l*] positions appear in the [1$\bar{1}$0] SAED pattern (marked with white arrowheads in Figure S7d, Supporting Information). These lines are reminiscent to those due to "honeycomb" Li and transition metal ordering in the Li-rich NMC oxides and can tentatively be attributed to the intralayer ordering of the alkali cations and vacancies in NKCM. [010] HAADF-STEM image of NKCM (**Figure 2a**) reveals that the P2 stacking remains, but instead of equidistant cationic layers in NCM, NKCM is characterized by the pattern of alternating short (≈5.6 Å) and long (≈6.2 Å) interlayer distances (Figure 2e). Atomic resolution STEM-EDX maps demonstrate that this alternation is caused by ordering of the Na and K cations into separate layers (Figure 2f). Following the symmetry analysis with ISODISTORT,[20] this ordering causes symmetry reduction from $P6_3/mmc$ to $P\bar{6}m2$ (*k*-vector [0,0,0], Γ_4^- irreducible representation). This ordering is, however, not perfect being occasionally violated with insertion of double Na layers (Figure S9, Supporting Information), in agreement with diffuse shape of the 00*l*, $l \neq 2n$ reflections in the SAED patterns of NKCM.

Continuation of the cation exchange results in further increase of the K content and amount of cation vacancies. However, sodium is not eliminated completely in the final KCM material resulting in the cation ratio of Na:K:Co:Mn = 0.04(1):0.293(4):0.336(4):0.664(5) ($(Na,K)_{1/3}Co_{1/3}Mn_{2/3}O_2$), which aligns well with the ICP-OES values of 0.025, 0.33, 0.31, and 0.67 for Na, K, Co, and Mn respectively. Thus, the KCM material contains twice less alkali cations compared to that in the parent NCM one. In the SAED patterns of KCM (Figure S7e,f, Supporting Information), the elongated shape of the 00*l*, $l \neq 2n$ reflections and diffuse streaks along c* through the main reflections of the P2 structure

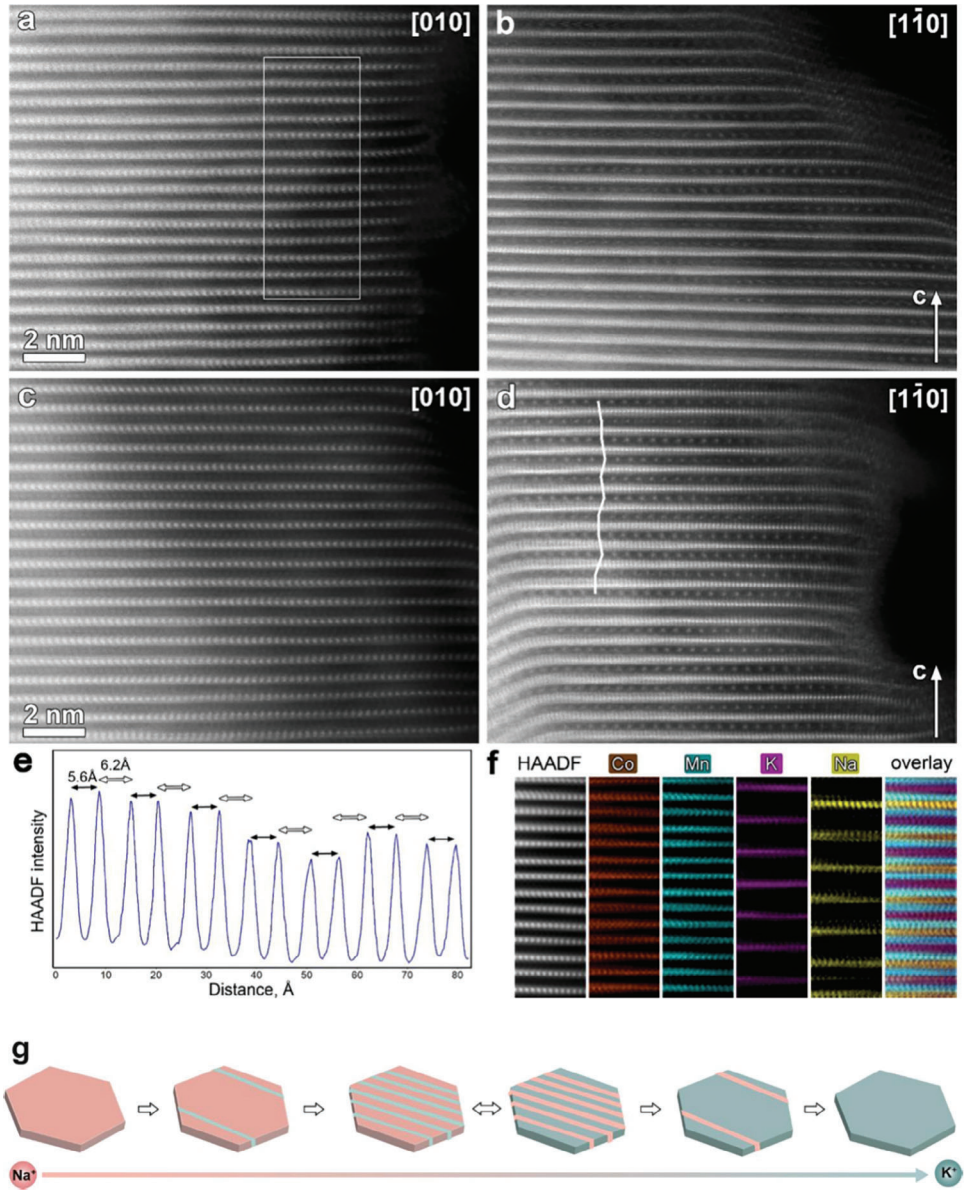

Figure 2. [010] and [1$\bar{1}$0] HAADF-STEM images of the a,b) intermediate NKCM phase and c,d) the final KCM phase. e) HAADF intensity profile along the rectangular area outlined in the panel (a) with the marked short (≈5.6 Å) and long (≈6.2 Å) interlayer distances. f) [010] HAADF-STEM image of NKCM and atomic resolution STEM-EDX maps demonstrating alternating Na and K layers. g) A schematic diagram illustrating the sequence of ion-exchange steps of Na^+–K^+ exchange mechanism during the *chimie douce* process.

disappear indicating suppression of the Na/K intralayer ordering. Indeed, in the [010] HAADF-STEM image, all cationic layers become equidistant again (Figure 2c). Contrarily, the ±n/3[11*l*] diffuse intensity lines become more intense (Figure S7f, Supporting Information). This ordering manifests itself in the [1$\bar{1}$0] HAADF-STEM image (Figure 2d) as a pattern of prominently bright dots in the alkali layers tripling the apparent repeat period along the layers. This tripled periodicity has perfect 2D ordering, but shifted randomly on going from layer to layer by 1/3 of the interdot distance (as marked with a zig-zag line in Figure 2d). Highly faulted arrangement of the ordered alkali layers along the c-axis causes diffuse intensity lines in the [1$\bar{1}$0] SAED pattern. This superstructure can be attributed to 2D ordering of one K and two cation vacancies (neglecting the minor Na content). One such ordered variants can be realized in the *P*6$\bar{c}$2 (*k*-vector [1/3,1/3,0], K_1 irreducible representation, the unit cell transformation matrix (by rows): (2,1,0) (−1,1,0) (0,0,1)).

Figure 2g schematically captures the complete ion-exchange process. Initially, the process involves replacing all the Na^+ in a few layers with K^+ and vacancies. Importantly, K and Na cannot occupy the same layer in order to minimize the intralayer lattice strain. As the reaction progresses, the number of K layers increases over time. In the midway point, alternating ordered layers of Na and K start to form. Concurrently, the number of Na layers

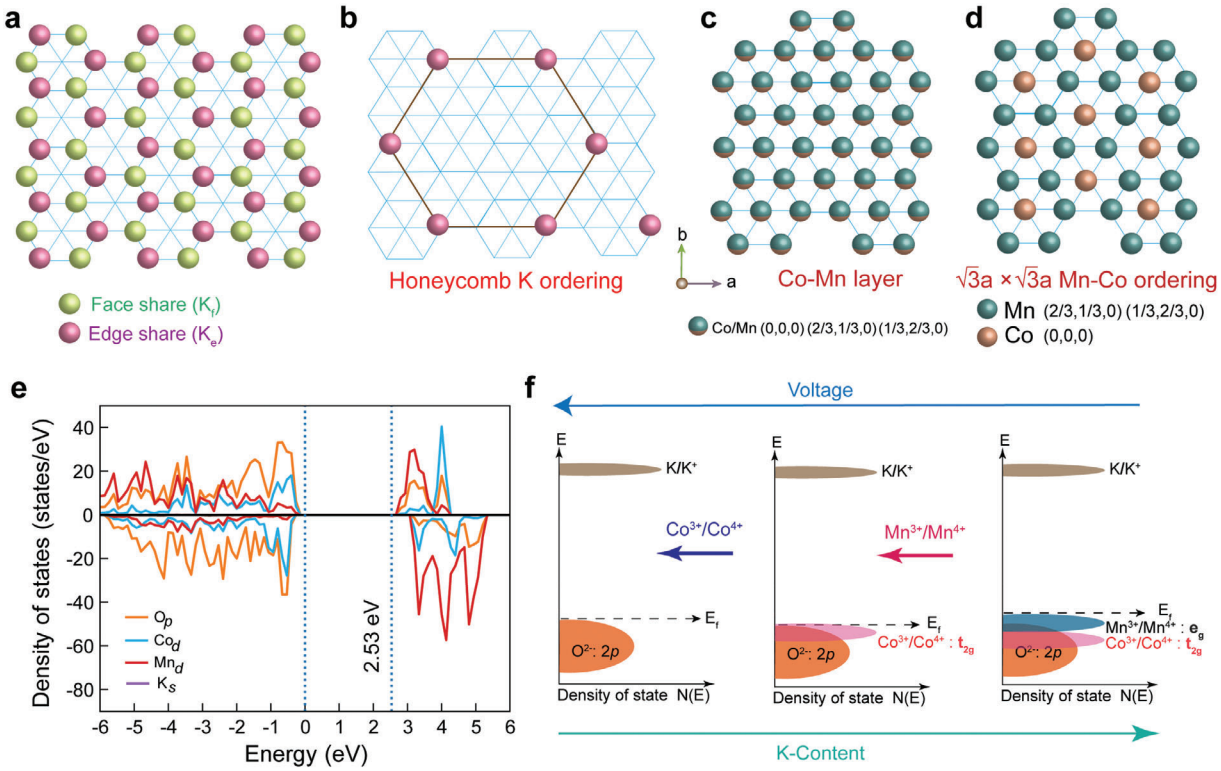

Figure 3. a) Illustration depicting various triangular prismatic sites (green: face shared prismatic sites K_f and pink: edge shared prismatic sites K_e) available for K-occupation within each K-layer in P2-type K_xMO_2 (M = transition metal(s)) crystal structure. b) Honeycomb ordering of edge shared (K_e) sites for P2-type $K_{1/3}Co_{1/3}Mn_{2/3}O_2$ compound in each K-layer. c) Possible sites for the Co and Mn viewed from the top along [001] direction. d) In-plane ground state of Co–Mn ordering in P2-type $K_{1/3}Co_{1/3}Mn_{2/3}O_2$. e) The density of state (DOS) for P2-KCM, as calculated by SCAN+*U*. Orange, blue, red, and purple curves correspond to the O *p*, Co *d*, Mn *d*, and K *s* states, respectively. The dotted blue lines are valence and conduction band edges. The energy scale is defined relative to the valence band maximum, and the bandgap is indicated by the text at the conduction band edge. f) Visualization of involvement of Mn 3*d*, Co 3*d*, and O 2*p* states in the (de)insertion process K^+ across different states of potassiation.

decreases with reaction time, while K layers increase. Toward the end of the reaction, there are only a few layers of Na remaining within the K-based lattice framework. Finally, all alkali layers are occupied by K^+ in a specific ordered pattern of K^+ and vacancy. Note that the diffusion of both alkali ions within the layered structure is rapid, leading to the formation of the end phase primarily governed by the thermodynamic stability of the final phase.

2.2. Computational Studies

We have performed density functional theory (DFT) calculations using the Hubbard *U* corrected strongly constrained and appropriately normed (SCAN+*U*) exchange-correlation functional to explore the KCM phase at the electronic scale.[21] Table S4 (Supporting Information) compiles the calculated lattice parameters and volumes, revealing a 0.35% and 8.38% deviation in calculated versus experimental values for lattice parameters "*a*" and "*c*", respectively, indicating close alignment of computed values with experiments. The underestimation of the "*c*" parameter by computation can be attributed to the limitations of the DFT framework in adequately capturing the van der Waals interactions between the large interlayer spacing across the K-layer. Additionally, the calculated bond lengths for Co and O suggest that even for the same electronic state of transition metal, the bond lengths are strongly dependent on K-content in the crystal structure (Figure S10, Supporting Information). Further, we observe, for the KCM phase, all the K^+ to occupy the edge shared triangular prismatic sites such that it forms a typical honeycomb superstructure across all K-layers (**Figure 3**a,b), which can be attributed primarily to the minimization of electrostatic repulsions. However, for the $K_{2/3}Co_{1/3}Mn_{2/3}O_2$ compound 54% of K^+ occupy by the face-shared prismatic sites, with the remaining K^+ occupying the edge-shared prismatic sites. Note that the edge-shared prismatic sites exhibit lower electrostatic repulsions between the K^+ and transition metal ions, while the face-shared sites reduce $K^+ - K^+$ repulsions. Thus, at higher K^+ concentrations, minimizing the repulsions between K^+ ions takes precedence, facilitating K^+ to occupy the face-shared prismatic sites in addition to the edge-shared sites.

Calculated on-site magnetic moments (Table S5, Supporting Information) indicate that in $K_{1/3}Co_{1/3}Mn_{2/3}O_2$, all Co ions exhibit a 3+ oxidation state, while all the Mn ions are in the 4+ state. The electrostatic interactions among Mn^{4+}, Co^{3+}, and K^+ ions vary due to differences in their sizes and electronic valence states, potentially resulting in ordering within the transition metal layers. Indeed, the DFT-relaxed structure reveals that there is

preferential occupancy of Co and Mn within the MO_2 sheets, strongly correlated to the K-content in the crystal lattice. Importantly, we observed the $\sqrt{3}a \times \sqrt{3}a$ in-plane transition metal Mn–Co ordering (Figure 3c,d) for the KCM phase, as reported in the case of Na-based layered compounds in previous studies.[22] For the higher K content $K_{2/3}Co_{1/3}Mn_{2/3}O_2$, another distinct configurational arrangement of Co–Mn emerges. In the transition metal layer adjacent to the basal layer (i.e., top layer), rows of Co ions are separated by two Mn rows (Figure S11, Supporting Information). In the basal transition metal layer, rows of Mn and Co are separated by an interwoven Co–Mn row (Figure S11, Supporting Information). In the fully depotassiated ($Co_{1/3}Mn_{2/3}O_2$) phase, the basal plane exclusively comprises Mn^{4+} ions while the top plane features alternate rows of interwoven Mn^{4+} and Co^{4+}.

To elucidate the redox mechanism, we analyzed the SCAN+*U*-calculated on-site magnetic moments for Mn and Co ions in pristine (KCM), potassiated ($K_{2/3}Co_{1/3}Mn_{2/3}O_2$) and fully charged ($Co_{1/3}Mn_{2/3}O_2$) phases, listed in Table S5 (Supporting Information). In the KCM phase, all Co ions exhibit a 3+ oxidation state and all Mn are in 4+ electronic states while in $K_{2/3}Co_{1/3}Mn_{2/3}O_2$, half of the Mn ions are distributed between 3+ and 4+ oxidation states and all the Co ions are in the 3+ electronic state. This suggests that Mn exhibits redox-activity while exchanging K across the KCM and $K_{2/3}Co_{1/3}Mn_{2/3}O_2$ compositions. Upon K^+ deintercalation from KCM forming the charged $Co_{1/3}Mn_{2/3}O_2$ phase, the on-site magnetic moments of Co show a significant change, indicating a Co^{3+} to Co^{4+} oxidation, while the magnetic moment of Mn ions changes marginally. Also, we don't observe any significant changes in the magnetic moments of the oxygen ions during K^+ (de)intercalation from the KCM phase. These observations collectively suggest the involvement of a purely cationic-redox K-storage mechanism within the KCM composition considered here.

Figure 3e and Figure S11c,d (Supporting Information) present the SCAN+*U*-calculated projected Density of States (pDOS) for the pristine (KCM), potassiated ($K_{2/3}Co_{1/3}Mn_{2/3}O_2$) and fully charged ($Co_{1/3}Mn_{2/3}O_2$) phases, respectively. The pDOS analysis reveals a semiconducting electronic structure for all compounds, revealing predicted bandgaps of 2.53, 1.28, and 1.70 eV, respectively. In the KCM structure, the Co 3*d* and O 2*p* bands dominate the valence band edge (VBE), while the Mn 3*d* states reside in the conduction band edge (CBE), suggesting the predominant participation of Co during K-removal. Notably, in the fully charged state, the contribution of Co *d* states in the VBE (CBE) is lower (higher) than the KCM compound, implying a shift of the Co *d* states from the occupied to unoccupied states, corresponding to the oxidation of Co during the de-potassiation process. During the discharge process, we observe a shift in the Mn *d* states from the CBE in the KCM phase to the VBE in the $K_{2/3}Co_{1/3}Mn_{2/3}O_2$ composition, suggesting Mn reduction. Thus, our pDOS calculations are consistent with the trends elucidated by our calculated on-site magnetic moments. In summary, our DFT calculations suggest that the electrochemical cycling process involves first oxidation of Mn at lower voltage ($K_{2/3}Co_{1/3}Mn_{2/3}O_2$ ↔KCM), followed by the subsequent oxidation of Co^{3+} to Co^{4+} (KCM ↔ $Co_{1/3}Mn_{2/3}O_2$) as schematically summarized in Figure 3f. These findings support the ex-situ XPS and electrochemical measurements as discussed in the following sections.

2.3. Electrochemical Analyses

To evaluate the electrochemical characteristics of P2-KCM versus K/K^+, we first conducted cyclic voltammetry (CV) measurements at a scan rate of 0.05 mV s^{-1} within two distinct potential ranges: 4.2 to 1.5 V and 4.2 to 2.0 V as presented in **Figure 4**a,b respectively. During the initial anodic scan, corresponding to K^+ deintercalation, the CV curves exhibit two well-resolved peaks at 3.83 V (labeled as O1) and 3.12 V (O2). Emergence of both the peaks can be attributed to the $Co^{3+/4+}$ redox process and possible structural cation ordering. In the subsequent oxidation cycle, two additional distinct peaks emerge at lower potentials, specifically at 2.45 V (O3) and 2.07 V (O4), which is associated solely to the Mn redox reactions, consistent with the previous electrochemical behavior of Mn-based layered oxide system, within the broader potential range of 4.2 to 1.5 V. During the cathodic scan, corresponding to K^+ insertion reaction, four peaks appear at 3.66 V (R1), 2.86 V (R2), 2.17 V (R3), and 1.81 V (R4). These peaks signify the reduction of both Co and Mn at high and low voltage ranges, respectively. Notably, within the narrow potential window of 4.2 to 2.0 V, the absence of a peak at 2.07 V is observed, which is associated with the $Mn^{2+/3+}$ redox couple. Further, it is noted that the peak shifts during reduction and oxidation reactions in subsequent cycles, reflecting the slight change in the potential for the respective electrochemical process compared to the first cycle. The CV curves are notably superposed during subsequent cycling, indicating the excellent electrochemical reversibility of the material. Additionally, the observed broader peaks suggest a topotactic K^+ (de)insertion reaction, highlighting the robust electrochemical performance within the selected potential windows. In addition, CV test was conducted at various scan rates in the range of 0.1 to 0.7 mV s^{-1} in K-half cell, as presented in Figure S12 (Supporting Information), showing the increase in peak currents with the scan rate.

Following, the potassium half-cells (K *vs.* KCM) were subjected to galvanostatic (dis)charge at a scan rate of 0.05 C (C/20), utilizing 0.5 M KTFSA in $Pyr_{13}TFSA$ electrolytes. At 25° C, P2-KCM material delivers a reversible capacity of ≈70 mAh g^{-1} (0.26 moles of K^+) within the potential range of 4.2–2.0 V and ≈98 mAh g^{-1} (0.37 moles of K^+) within the potential window of 4.2 to 1.5 V, as displayed in Figure 4. Importantly, the initial discharge capacity exceeds the charge capacity, indicating that, during the first battery cycle of the KCM host framework, more potassium ions are inserted than removed. The voltage curve of KCM shows multiple small working plateaus during K^+ ion (de)insertion, aligning with the redox peaks evident in the CV profiles. Moreover, the cathode demonstrates an average voltage of 2.9 and 2.7 V within the electrochemical potential windows of 4.2 – 2.0 V and 4.2 – 1.5 V, respectively. Additionally, we observe nearly 93% capacity retention, commendable rate capability, and almost perfect (100%) coulombic efficiency after the 100th cycle in the narrower voltage range. This underscores the excellent electrochemical reversibility and robust structural integrity of the host framework. However, within the broader potential range, 74% capacity retention and 98% Coulombic efficiency were noticed after the 100th cycle.

The potassium storage capabilities of the P2-KCM host were examined in temperature controlled environments, specifically at 40 and 50 °C, as represented in **Figure 5** and Figure S13

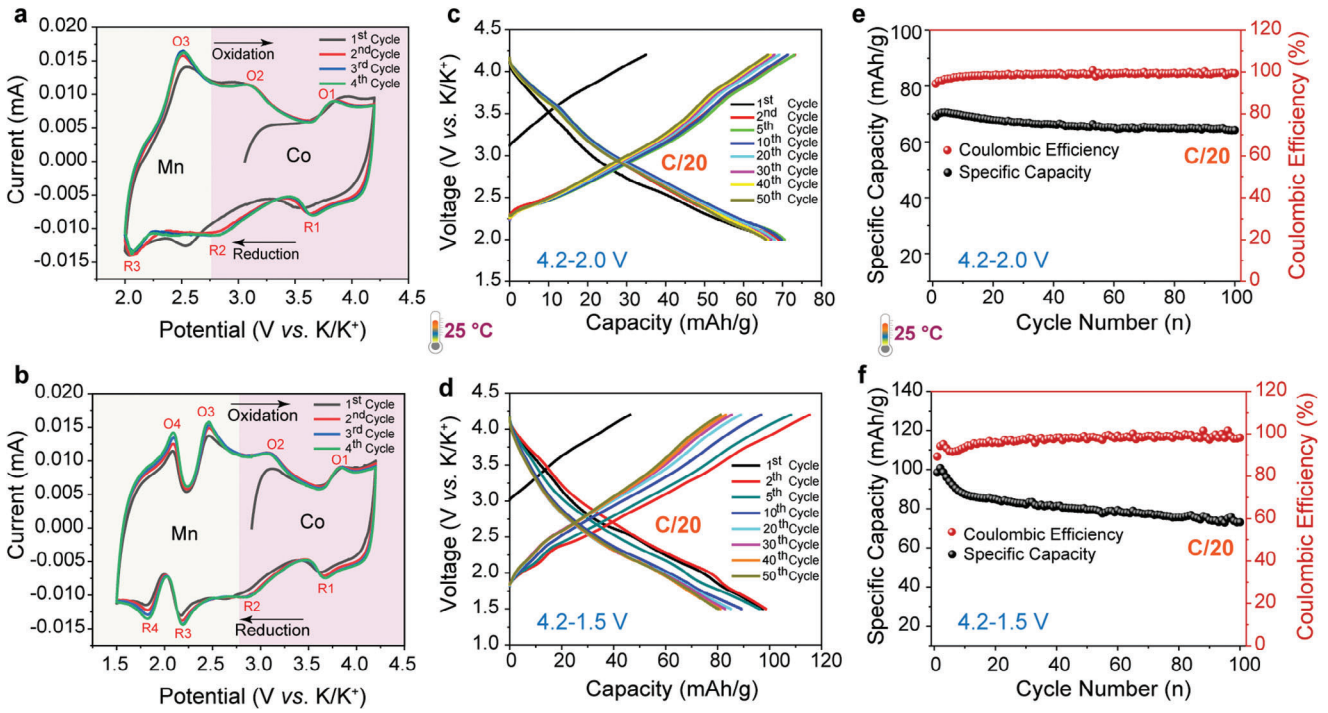

Figure 4. K^+ storage properties of KCM at room temperature (25 °C). Cyclic voltammograms (CV) of as prepared KCM cathode in K-half cell versus K/K^+ at scan rates of 0.1 mV s^{-1} in two different selected voltage windows: a) 4.2 – 2 V, and b) 4.2 – 1.5 V. Galvanostatic (dis)charge profiles at a current rate of C/20 across a potential window range of 4.2 – 2.0 V c) and 4.2 – 1.5 V d). e,f) specific discharge capacity and coulombic efficiency up to 100th cycles at a current rate of C/20.

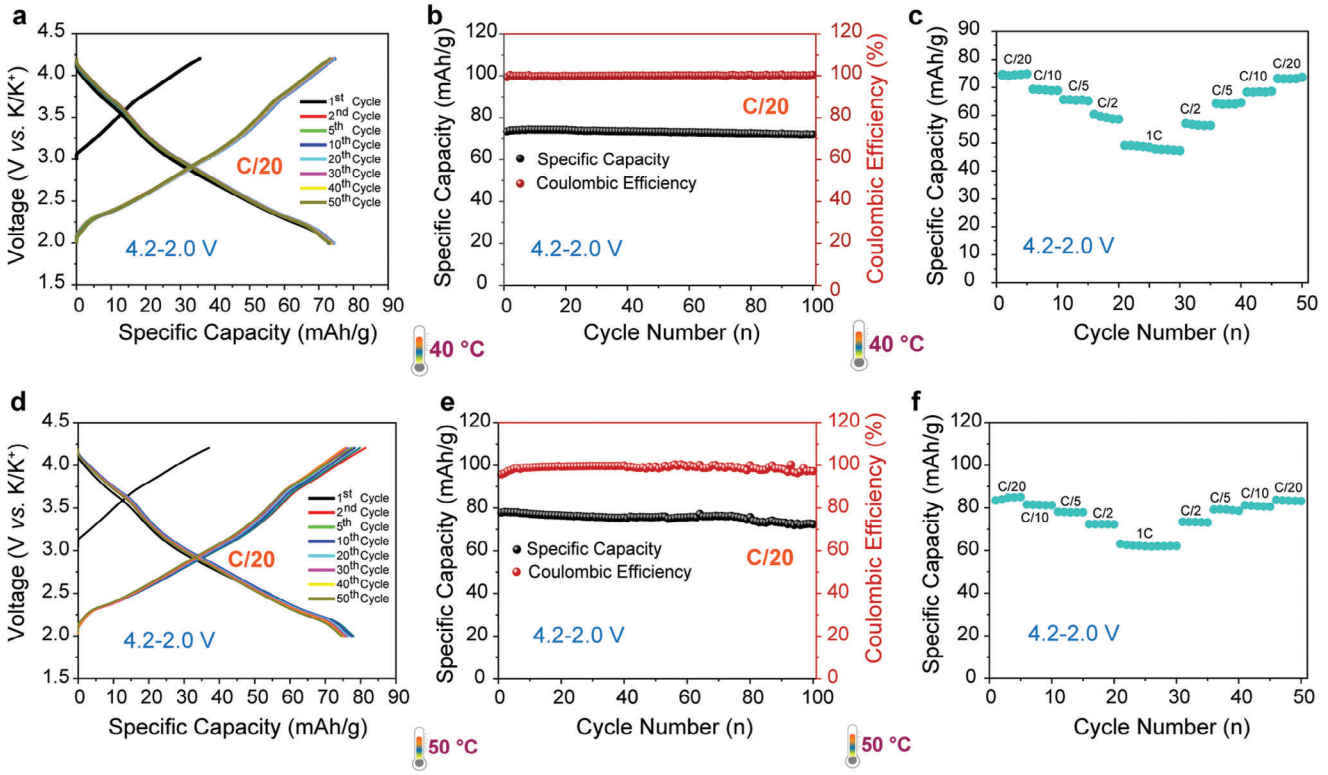

Figure 5. K^+ storage properties of the KCM phase at elevated temperatures of a–c) 40 °C and d–f) 50 °C across a potential window of 4.2 – 2.0 V. (a and d) Galvanostatic (dis)charge profiles at a current rate of C/20, (b and e) specific discharge capacity and coulombic efficiency up to 100th cycles at a C/20 current rate, and (c and f) rate stability at different current rates.

(Supporting Information). Notably, at 40 °C, we found the initial discharge capacity was ≈74 mAh g^{-1} (0.29 mole of K^+) and ≈115 mAh g^{-1} (0.43 mole of K^+) at the current rate of C/20. Further, during cycling tests at a current rate of C/20, the material showed exceptional performance, 97% (79%) discharge capacity retention with 100% (94%) coulombic efficiency after the 100th battery cycle, highlights the ability of the P2-KCM material to maintain cycling performance under elevated temperature conditions. Moreover, the rate performance data indicate the cathode consistently retains its ability to store and release K^+ ions over multiple cycles at various current rates. For instance, at different current rates such as C/20, C/10, C/5, C/2, and 1C, it delivers capacities of 74 (115), 69 (107), 65 (100), 59 (79), and 47 (48) mAh g^{-1}, respectively (as shown in Figure 5c; Figure S13c, Supporting Information). Furthermore, when the current is returned to C/20, a reversible capacity of 106 mAh g^{-1} can be regained. This suggests that the material has a remarkable tolerance for the rapid movement of K^+ ions in and out of its structure. It's important to note that capacity losses are more noticeable when using a broader potential range, regardless of temperature. This indicates that the redox reactions involving $Mn^{3+/2+}$ contribute to the decrease in capacity over time.

Additionally, at 50 °C, the P2-KCM host demonstrated first discharge capacities of ≈80 and ≈126 mAh g^{-1}, signifying the participation of 0.30 and 0.47 moles of K^+ during electrochemical reaction when the lower voltage cut-off was constrained to 2.0 and 1.5 V, respectively. For 100 cycles, the material exhibited an impressive capacity retention of 94% (73%) within the potential window of 4.2–2.0 V (4.2–1.5 V), coupled with high coulombic efficiency values of 97% (95%). These outcomes further demonstrate the excellent electrochemical reversibility of the cathode material at elevated temperature. Notably, the rate performance at high temperatures was excellent in both potential windows, as depicted in Figure 5f and Figure S13f (Supporting Information); the cathode material consistently maintains its ability to store and release K^+ over multiple cycles at different current rates. Specifically, it delivers discharge capacities of 84 (125), 81 (117), 77 (107), 72 (88), and 61 (70) mAh g^{-1} when subjected to current densities of C/20, C/10, C/5, C/2, and 1C, respectively in the voltage window of 4.2–2.0 V (4.2–1.5 V). Upon returning the current density back to C/20, the cathode shows an impressive recovery, achieving a rechargeable capacity of 83 and 130 mAh g^{-1} in the narrow and broader voltage window, respectively. Thus, the target cathode can undergo rapid K^+ (de)insertion attesting its excellent performance under varying charging conditions in harsh conditions.

2.4. (De)Potassiation Redox Mechanism

To probe the underlying K^+ storage mechanism during the (dis)charge cycles, we utilized ex situ X-ray powder diffraction (XRD) at different stages of (de)potassiation. These stages included the pristine P2 KCM state, the end of the first charge cycle (4.2 V), and the discharge to 3.5, 3.2, 2.0 and 1.5 V, as depicted in **Figure 6a**. The resulting XRD patterns at various (de)potassiation stages displayed gradual peak shifts when K^+ ions were (de)inserted, suggesting a solid solution (single-phase) redox reaction. As K^+ were extracted during charging, the reflections of the first three peaks of KCM shifted toward lower angles. This shift was accompanied by an increase in the *d*-spacing (Table S6, Supporting Information), indicating an increase in electrostatic repulsion between the electron density of oxygen atoms within the adjacent MO_6 layers. All these peaks shifted back to higher 2θ values as K^+ ions intercalated into the KCM framework on discharge. Importantly, shifting of peaks toward higher angles was observed compared to the pristine sample, when the discharge voltage reaches 2 and 1.5 V. It suggests a greater incorporation of K^+ into the crystal structure than the initial material. This shift brought the *d*-spacings back to their lower value, pointing to the high structural stability of KCM host material during electrochemical extraction and insertion of K^+ ions. Importantly, the inclusion of Co^{3+} within the crystalline matrix serves to alleviate the proclivity for irreversible phase transitions at elevated voltages, a prevalent attribute commonly observed in Mn-based systems.

Further, to examine the oxidation states of Co, Mn, and O at pristine and (dis)charged states, ex-situ XPS measurements were recorded. Figure 6b,c illustrate the XPS spectra of the Co2*p* and Mn 2*p* core levels for the as-synthesized P2-KCM sample, following to charging to 4.2 V, and after discharging to both 2.0 and 1.5 V, respectively. Upon charging to 4.2 V, the Co 2*p* spectrum shifts toward slightly lower binding energies, with a significant reduction in the relative area of Co $2p_{3/2}$ satellite peak, indicating oxidation of Co from 3+ to 4+ state (Tables S1 and S7, Supporting Information).[23] However, the Mn 2*p* spectrum remains unchanged, indicating the inactivity of Mn during first charging process. During discharging to 2.0 V, Mn 2*p* spectra shift toward lower binding energies, indicating a reduction in oxidation states from Mn^{4+} to Mn^{3+}. Moreover, the increase in the relative shake-up satellite peak area of Co $2p_{3/2}$, along with a reduction in full width at half maximum (f.w.h.m) from 3.1 to 1.68 eV, confirms the reduction of Co^{4+} to Co^{3+}. Upon further discharging to 1.5 V, the Co 2*p* spectrum remains unchanged, suggesting stability in the oxidation state. In contrast, changes in the Mn spectrum indicate a transition from Mn^{3+} to Mn^{2+}, confirming the exclusive Mn redox activity in the low-voltage redox region. Through the (dis)charging process, we do not observe any visible change in O 1*s* spectra (Figure S14, Supporting Information), confirming the electrochemical inactivity of O ions (i.e., anionic redox activity) in P2-KCM.

To gain insight of structural dynamics during K^+ (de)insertion at the atomic level, we conducted ex-situ TEM analysis of KCM cathode. Examination of the SAED patterns revealed diffraction spots consistent with a hexagonal crystal system, in alignment with the underlying solid solution reaction mechanism during (de)potassiation. Notably, both the charged and discharged phases consistently exhibited superlattice spots alongside regular spots, indicative of in-plane $\sqrt{3}a \times \sqrt{3}a$ Co–Mn ordering, highlighted by blue circles (Figure 6d–f). Additionally, analyzing the SAED spots, we observed a slight decrease in the *d*-spacing of the (110) plane from 2.46 Å during the charge phase, to 2.44 Å. Conversely, during discharge at voltages of up to 2.0 and 1.5 V, the d-spacing increased to 2.48 and 2.52 Å, respectively. This small change in *d*-spacing directly correlates with the concentration of potassium within the KCM phase. High-resolution TEM (HRTEM) images of all samples displayed clear lattice fringes corresponding to specific planes, reinforcing the

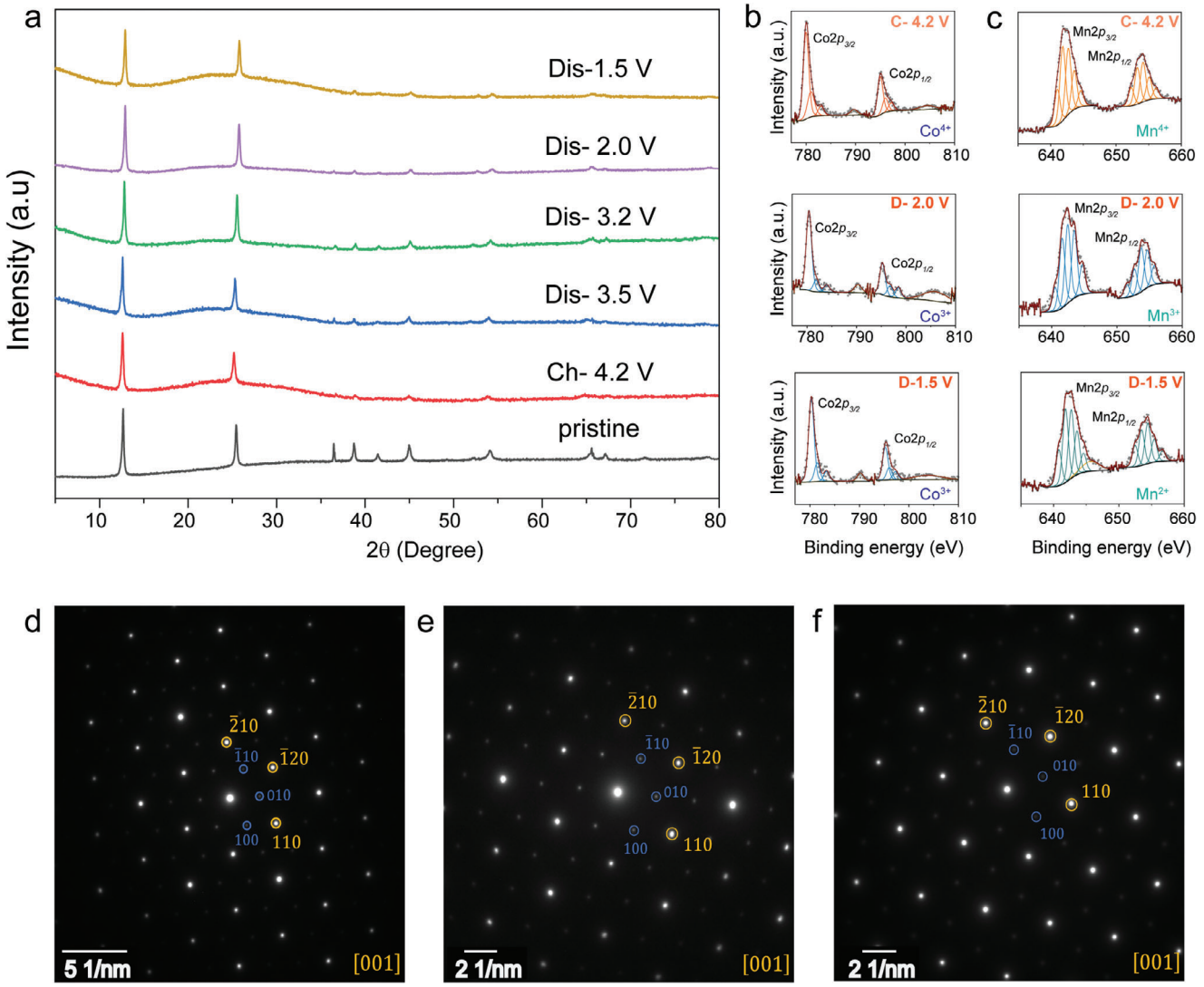

Figure 6. Comparative (left) ex-situ powder X-Ray diffraction patterns of KCM cathode versus K/K^+ at different states of (dis)charge. b,c) High-resolution XPS spectra for KCM probing b) Co 2*p* and c) Mn 2*p*. The rows indicate different states of (de)potassiation, namely charged (at 4.2 V, top row), pristine KCM (2nd row from top), discharged (at 2.0 V, 3rd row from top), and discharged (at 1.5 V, bottom row). The shifting of the Co and Mn peaks toward higher (lower) binding energy at the charged (discharged) states confirm the change in the redox state of Co and Mn. SAED patterns of KCM cathode at different states of (de)potassiation along c direction: d) charged to 4.2 V, e) discharged to 2.0 V, and f) discharged to 1.5 V. In each case, superstructure peaks are highlighted by blue circles, and yellow circles represent the regular spots. The indexing of the SAED patterns were performed using the supercell of size $\sqrt{3}a \times \sqrt{3}a$.

structural integrity of KCM throughout the K^+ (de)insertion process (Figure S15, Supporting Information).

3. Conclusion

Addressing intricate synthetic challenges associated with K-based cathodes, we employed the ambient (*chimie douce*) ion-exchange synthesis to discover a novel P2-type $K_{1/3}Co_{1/3}Mn_{2/3}O_2$ (KCM) cathode material for KIBs, potentially suitable for stationary storage applications. Integrating diffraction and spectroscopy techniques, we have elucidated the ion exchange reaction proceeds via an overlay ordered structure formation mechanism. Additionally, we have demonstrated the structural, morphological, electronic, and electrochemical properties of the ion-exchanged KCM material. This material works as a robust 2.9 V potassium insertion host, exploiting the Co and Mn redox centers. This KCM cathode involves Co–Mn in-plane ordering (leading to superstructure) and solid-solution redox mechanism during K^+ (de)insertion. It showcases exceptional structural reversibility, enduring cycling performance, and maintains nearly full coulombic efficiency even after 100 cycles, both in ambient and high temperature conditions. Synergy of first principles calculations with experimental characterizations unveiled the efficacy of ambient ion-exchange reactions in synthesizing highly promising cathode materials. Finally, this work also provides a new dimension in obtaining targeted battery material beyond

traditional synthetic routes for the development of KIBs for stationary energy storage systems.

4. Experimental Section

Material Synthesis: The soft chemistry (*chimie douce*) synthesis route was employed to derive the desired P2-type $K_{1/3}Co_{1/3}Mn_{2/3}O_2$ (KCM) phase from the parent P2 $Na_{2/3}Co_{1/3}Mn_{2/3}O_2$ (NCM) phase. Prior to the ion-exchange process, the NCM compound was prepared using a fuel (citric acid) assisted solution combustion route. Initially, low-cost metal nitrates oxidizers, $NaNO_3$ (SDFCL, 99.5%), $Mn(NO_3)_2.4H_2O$ (Thermo Fisher Scientific, 98%), and $Co(NO_3)_2.6H_2O$ (SDFCL, 99%) in the molar ratio of 2/3:1/3:2/3 respectively and citric acid (SDFCL, 99.5%) as a fuel were dissolved in minimal quantity of distilled water. This precursor solution was subjected to heating at 120 °C to induce solvent evaporation and formation of a densified gel. Subsequently, the gel was transferred to a higher temperature (200 °C) plate to initiate combustion reaction, which gradually facilitated the conversion of the material into a fluffy black intermediate complex. The obtained black power was mildly ground and was annealed at 900 °C for 6 h (in air) to yield the targeted parent P2 type NCM phase. Following, the as prepared NCM (1 g) powder was mixed with a molar excess of potassium ions, precisely ten times the stoichiometric quantity, achieved by dissolving KNO_3 in 50 ml of deionized water. The resulting mixture was continuously stirred for 8 h in ambient condition as presented in Figure S1 (Supporting Information). This methodology represents a simple soft chemistry approach conducted at room temperature with a goal of transforming sodium-based layered materials into their potassium analogs.

Structural and Physical Characterizations: The crystal structures of both the NCM and KCM phases were determined using a PANalytical X'pert pro diffractometer equipped with Cu K_α ($\lambda_1 = 1.5405$ Å, $\lambda_2 = 1.5443$ Å) source. The X-ray generator was operated at 40 kV/30 mA, and a Ni-filter was utilized as a monochromator. Rietveld refinement was carried out with the FullProf suite and the resulting crystal structures were illustrated using the VESTA-3 software.[24] The particle morphology was analyzed using a Carl Zeiss Ultra55 field emission scanning electron microscope (FESEM) unit with a thermal field emission-type tungsten source operating in the range of 0.1–20 kV. The spatial elemental distribution was investigated using an energy-selective backscattered detector at 15 kV in both line and area scan modes. The stoichiometry of KCM phase was determined using an an Ametek SPECTRO ARCOS inductively coupled plasma optical emission spectrometer (ICP-OES). For the analysis, the powder sample underwent a complete digestion in a microwave after being treated with aqua regia. Ultraviolet Photoelectron Spectroscopy (UPS) was conducted using the ULVAC-PHI 5000 Versa Probe III within a standard ultra-high vacuum chamber (pressure: 5×10^{-10} mbar). It employed a helium (He1) photon source with an energy of 21.2 eV, a maximum beam power of 100 W, and a beam voltage of 500 V. The current was maintained at 100 mA, and the pass energy was set to 1.3 eV with a step size of 0.005 eV.

Transmission Electron Microscopy: TEM samples were prepared by crushing the crystals with an agate mortar and pestle in dimethyl carbonate and depositing drops of suspension onto a carbon film supported by a copper grid. Samples for TEM were stored and prepared in an MBraun LabStar GmbH Ar-filled glovebox to minimize exposure to air. A Gatan vacuum transfer holder was used to transport the samples from the glove box to the microscope column. Selected area electron diffraction (SAED) patterns, high angle annular dark field scanning transmission electron microscopy (HAADF-STEM) images as well as energy-dispersive X-ray (EDX) spectra and maps in the STEM mode (EDX-STEM) were acquired on a probe aberration-corrected ThermoFisher Titan Themis Z electron microscope at 200 kV equipped with a Super-X system for EDX analysis. Ex situ TEM was performed using an FEI Tecnai T20 ST electron microscope (operated at 200 kV) equipped with a double-tilt holder.

Electrochemical Measurements: A working electrode sheet for assessing electrochemical performance was prepared from the intimate mixture of vacuum dried KCM active material, ketjen black (KB) and teflonized acetylene black (TAB) binder in 75:15:10 ratio respectively inside an Ar-filled glove box (MBraun LabStar GmbH, O_2 and H_2O level maintained below 0.5 ppm) to avoid any moisture/oxygen contamination. Either CR2032 coin-type half-cells or swagelok cells were assembled using potassium metal foil as counter and reference electrode, which are separated from working electrode sheet by using glass fiber separator (Whatman, GF/C) soaked in 0.5 M KTFSI (bis(trifluoromethanesulfonyl)imide) salt in Pyr13TFSI in (1-methyl-1-propylpyrrolidinium bis(trifluoromethanesulfonyl) amide) acting as the electrolyte.[25] Typical active material loading was ≈3–5 mg per electrode sheet.

Ex Situ Analyses: For ex situ analyses, Swagelok cells were cycled at different states of (dis)charge and were disassembled inside the Ar-filled glove box. Following, the cycled electrodes were retrieved and were cleaned using diethyl carbonate (DEC) and dried overnight. After drying, XRD patterns and XPS spectra were recorded at ambient condition. The XPS spectra were acquired using a Thermo-Scientific Kα XPS instrument operating at 12 kV/6 mA.

Computational Methods: The DFT calculations were conducted within Vienna ab initio simulation package (VASP), employing projector augmented wave (PAW) method to model the core electrons.[26] The SCAN+U functional was used for the exchange-correlation while incorporating U corrections of 2.7 and 3.1 eV for Mn and Co, respectively.[21] A dense Γ-centered Monkhorst–Pack k-point grid with a density of 32 k-points $Å^{-1}$ were used for the Brillouin zone integration.[27] The kinetic energy cutoff of plane waves was set to 520 eV. To integrate the Fermi surface, a Gaussian smearing with width of 0.05 eV was used. During structure relaxation, the conjugate gradient scheme was utilized with convergence criterion set at |0.01| eV $Å^{-1}$ for atomic forces and 10^{-5} eV for the total energy. Structure relaxations were performed without preserving any symmetry and the cell volume, the cell shape, and positions of all ions were relaxed.[28] The initial magnetic moment of Co and Mn were set assuming low-spin and high-spin ferromagnetic ordering, respectively. As the structure can exhibit various K-vacancy and Co-Mn arrangements, the pymatgen package was utilized to systematically enumerate all symmetrically unique K-vacancy and Co-Mn configurations.[29] Among the several possible ordered structures, the ones with the lowest energy, as determined by DFT, were chosen for further calculations and analyses.

Supporting Information

Supporting Information is available from the Wiley Online Library or from the author.

Acknowledgements

The current work was financially supported by the Department of Science and Technology (Government of India) under the Core Research Grant (CRG/2022/000963). The authors thank Dr. K. Yoshii and Dr. T. Masese (AIST, Osaka, Japan) for providing K-based electrolyte and R. Vengarathody for help with ICP-OES analysis. P.K.J. and D.S. are grateful to the Ministry of Human Resource Development (MHRD, Government of India) for financial assistance. G.S.G. acknowledges financial support from the Science and Engineering Research Board (SERB) of the Government of India, under sanction numbers SRG/2021/000201 and IPA/2021/000007. P.K.J. and G.S.G. acknowledge the computational resources provided by the Supercomputer Education and Research Centre (SERC), IISc. Part of the microscopy work was performed at the the Advanced Facility for Microscopy and Microanalysis (AFMM, IISc). A.G. and A.M.A. are grateful to the Russian Science Foundation for financial support (grant 23-73-30003). A.G. and A.M.A. are grateful to Advanced Imaging Core Facility (AICF) at Skoltech for providing access to electron microscopy equipment. P.B. is grateful to the Alexander von Humboldt Foundation (Bonn, Germany) for a 2022 Humboldt fellowship for experienced researchers. This work contributes to the research performed at CELEST (Center for Electrochemical Energy Storage Ulm-Karlsruhe).

Conflict of Interest

The authors declare no conflict of interest.

Data Availability Statement

The data that support the findings of this study are available from the corresponding author upon reasonable request.

Keywords

cathodes, chimie douce, energy storage, P2 layer oxides, potassium-ion batteries

Received: June 18, 2024
Revised: July 17, 2024
Published online:

[1] M. Armand, J. M. Tarascon, *Nature* **2008**, *451*, 652.
[2] M. S. Whittingham, *Chem. Rev.* **2014**, *114*, 11414.
[3] a) T. Hosaka, K. Kubota, A. S. Hameed, S. Komaba, *Chem. Rev.* **2020**, *120*, 6358; b) N. Yabuuchi, K. Kubota, M. Dahbi, S. Komaba, *Chem. Rev.* **2014**, *114*, 11636.
[4] a) H. Kim, J. C. Kim, M. Bianchini, D.-H. Seo, J. Rodriguez-Garcia, G. Ceder, *Adv. Energy Mater.* **2018**, *8*, 1702384; b) J.-Y. Hwang, S.-T. Myung, Y.-K. Sun, *Adv. Funct. Mater.* **2018**, *28*, 1802938.
[5] S. Komaba, T. Hasegawa, M. Dahbi, K. Kubota, *Electrochem. Commun.* **2015**, *60*, 172.
[6] a) M. Okoshi, Y. Yamada, S. Komaba, A. Yamada, H. Nakai, *J. Electrochem. Soc.* **2017**, *164*, A54; b) Y. Matsuda, H. Nakashima, M. Morita, Y. Takasu, *J. Electrochem. Soc.* **1981**, *128*, 2552.
[7] C. Fouassier, C. Delmas, P. Hagenmuller, *Mater. Res. Bull.* **1975**, *10*, 443.
[8] X. Zhang, Z. Wei, K. N. Dinh, N. Chen, G. Chen, F. Du, Q. Yan, **2020**, *16*, 2002700.
[9] a) X. Wang, X. Xu, C. Niu, J. Meng, M. Huang, X. Liu, Z. Liu, L. Mai, *Nano Lett.* **2017**, *17*, 544; b) Z. Maider, C.-G. Javier, L. Michal, A. Henry, I. Boyan, J. S. S. Thomas, P. Stefano, C.-M. Elizabeth, *Energy Mater.* **2023**, *3*, 300046; c) Z. Xiao, F. Xia, L. Xu, X. Wang, J. Meng, H. Wang, X. Zhang, L. Geng, J. Wu, L. Mai, *Adv. Funct. Mater.* **2022**, *32*, 2108244; d) Z. Liu, X. Liu, B. Wang, X. Wang, D. Lu, D. Shen, Z. Sun, Y. Liu, W. Zhang, Q. Zhang, Y. Li, *eScience* **2023**, *3*, 100177; e) H. Zhou, Y. Bai, C. Yang, C. Guo, F. Liu, P. Hu, C. Han, X. Wang, *Chem. Eng. J.* **2024**, *488*, 150809.
[10] a) H. Kim, D.-H. Seo, A. Urban, J. Lee, D.-H. Kwon, S.-H. Bo, T. Shi, J. K. Papp, B. D. McCloskey, G. Ceder, *Chem. Mater.* **2018**, *30*, 6532; b) C. Delmas, M. Devalette, C. Fouassier, P. Hagenmuller, *Mater. Res. Bull.* **1975**, *10*, 393; c) Y. Hironaka, K. Kubota, S. Komaba, *Chem. Commun.* **2017**, *53*, 3693; d) M. Jansen, F. M. Chang, R. Hoppe, *Z. Anorg. Allg. Chem.* **1982**, *490*, 101.
[11] a) K. Sada, B. Senthilkumar, P. Barpanda, *Chem. Commun.* **2017**, *53*, 8588; b) M. G. T. Nathan, N. Naveen, W. B. Park, K.-S. Sohn, M. Pyo, *J. Power Sources* **2019**, *438*, 226992; c) J. H. Jo, J. U. Choi, Y. J. Park, Y. H. Jung, D. Ahn, T.-Y. Jeon, H. Kim, J. Kim, S.-T. Myung, *Adv. Energy Mater.* **2020**, *10*, 1903605.
[12] J.-Y. Hwang, J. Kim, T.-Y. Yu, S.-T. Myung, Y.-K. Sun, *Energy Environ. Sci.* **2018**, *11*, 2821.
[13] J. Gopalakrishnan, *Chem. Mater.* **1995**, *7*, 1265.
[14] C. Delmas, C. Fouassier, P. Hagenmuller, *Physica B+C* **1980**, *99*, 81.
[15] a) M. M. Claude Delmas, C. Fouassier, P. Hagenmuller, *Mater. Res. Bull.* **1976**, *11*, 1483; b) C. Zhao, Q. Wang, Z. Yao, J. Wang, B. Sánchez-Lengeling, F. Ding, X. Qi, Y. Lu, X. Bai, B. Li, H. Li, A. Aspuru-Guzik, X. Huang, C. Delmas, M. Wagemaker, L. Chen, Y. S. Hu, *Science* **2020**, *370*, 708.
[16] P. K. Jha, S. N. Totade, P. Barpanda, G. Sai Gautam, *Inorg. Chem.* **2023**, *62*, 14971.
[17] H. Kim, J. C. Kim, S.-H. Bo, T. Shi, D.-H. Kwon, G. Ceder, *Adv. Energy Mater.* **2017**, *7*, 1700098.
[18] T. Itoh, H. Sato, T. Nishina, T. Matue, I. Uchida, *J. Power Sources* **1997**, *68*, 333.
[19] C. Zhao, M. Avdeev, L. Chen, Y.-S. Hu, *Angew. Chem., Int. Ed.* **2018**, *57*, 7056.
[20] B. J. Campbell, H. T. Stokes, D. E. Tanner, D. M. Hatch, *J. Appl. Cryst.* **2006**, *39*, 607.
[21] a) J. Sun, A. Ruzsinszky, J. P. Perdew, *Phys. Rev. Lett.* **2015**, *115*, 036402; b) O. Y. Long, G. Sai Gautam, E. A. Carter, *Phys. Rev. Mater.* **2020**, *4*, 045401; c) G. Sai Gautam, E. A. Carter, *Phys. Rev. Mater.* **2018**, *2*, 095401.
[22] a) K. Kubota, T. Asari, S. Komaba, *Adv. Mater.* **2023**, *35*, 2300714; b) J. M. Paulsen, R. A. Donaberger, J. R. Dahn, *Chem. Mater.* **2000**, *12*, 2257.
[23] L. Dahéron, R. Dedryvère, H. Martinez, M. Ménétrier, C. Denage, C. Delmas, D. Gonbeau, *Chem. Mater.* **2008**, *20*, 583.
[24] a) J. Rodríguez-Carvajal, *Phys. B.* **1993**, *192*, 55; b) K. Momma, F. Izumi, *J. Appl. Cryst.* **2011**, *44*, 1272.
[25] K. Yoshii, T. Masese, M. Kato, K. Kubota, H. Senoh, M. Shikano, *ChemElectroChem* **2019**, *6*, 3901.
[26] a) P. Hohenberg, W. Kohn, *Phys. Rev. B.* **1964**, *136*, B864; b) W. Kohn, L. J. Sham, *Phys. Rev.* **1965**, *140*, A1133; c) G. Kresse, D. Joubert, *Phys. Rev. B.* **1999**, *59*, 1758; d) G. Kresse, J. Hafner, *Phys. Rev. B.* **1993**, *48*, 13115; e) G. Kresse, J. Furthmüller, *Phys. Rev. B.* **1996**, *54*, 11169.
[27] H. J. Monkhorst, J. D. Pack, *Phys. Rev. B.* **1976**, *13*, 5188.
[28] K. M. Ho, C. L. Fu, B. N. Harmon, W. Weber, D. R. Hamann, *Phys. Rev. Lett.* **1982**, *49*, 673.
[29] A. Jain, S. P. Ong, G. Hautier, W. Chen, W. D. Richards, S. Dacek, S. Cholia, D. Gunter, D. Skinner, G. Ceder, K. A. Persson, *APL Mater.* **2013**, *1*, 011002.